Journal of
Materials Chemistry A

Accepted Manuscript

This article can be cited before page numbers have been issued, to do this please use: G. Cheng, S. Xie, B. Lan, X. Zheng, F. Ye, M. Sun, X. Lu and L. Yu, *J. Mater. Chem. A*, 2016, DOI: 10.1039/C6TA04530H.

ROYAL SOCIETY OF CHEMISTRY

www.rsc.org/materialsA

View Article Online
DOI: 10.1039/C6TA04530H

Journal Name

ARTICLE

Received 00th January 20xx,
Accepted 00th January 20xx

DOI: 10.1039/x0xx00000x

www.rsc.org/

Phase Controllable Synthesis of Three-Dimensional Star-like MnO_2 Hierarchical Architectures as Highly Efficient and Stable Oxygen Reduction Electrocatalysts

Gao Cheng,[a] Shilei Xie,[b] Bang Lan,[c] Xiaoying Zheng,[a] Fei Ye,[a] Ming Sun,[a] Xihong Lu,[b]* and Lin Yu[a]*

To achieve high performance of fuel cells and metal-air batteries, searching the inexpensive and earth-abundant catalysts with enhanced activity and durability for oxygen reduction reaction (ORR) are currently pursued. Herein, three-dimensional (3D) α-MnO_2 and ε-MnO_2 hierarchical star-like architectures with tunable crystal phase and desirable ORR activity were readily prepared by a facile hydrothermal method without any surfactants or templates. The effects of reaction temperature, anion type and dwell time on the morphologies of the MnO_2 products were studied in detail, and the possible formation mechanism of the 3D MnO_2 hierarchical stars was proposed. Due to the improved electrical conductivity and O_2 adsorption ability, the resulting α-MnO_2 catalyst showed substantially enhanced ORR activity compared to the ε-MnO_2 and bulk MnO_2 catalysts, with a more positive onset potential, larger limiting current density and better durability. Our results provide a facile chemical route towards phase-controlled synthesis of the 3D MnO_2 architectures, which can be served as the efficient catalysts for ORR-based applications.

Introduction

The ever-growing demands for energy and environment protection have stimulated significant interests in the development of sustainable energy conversion and storage devices. Fuel cells and metal-air batteries are recognizing as the most promising energy conversion and storage devices for their theoretically high energy density and wide applications.[1-5] The essential to gain their optimal performance is to develop efficient electrocatalysts for the oxygen reduction reaction (ORR). Noble metal and its alloys are the most active ORR electrocatalysts,[6,7] but they are highly expensive and scarce. Alternatively, substantial efforts have been devoted to exploring the non-precious ORR electrocatalysts. Up to now, multifarious electrocatalysts such as transition-metal oxides,[8-10] doped carbons[11,12] and metal-N_4 chelates macrocycles[13] have been reported. Among them, manganese dioxide (MnO_2) holds great promise as alternative and cost-effective electrocatalyst for ORR due to its low cost, environmental friendliness, structural diversity (e. g., α-, β-, γ-, δ-, and ε- type, *etc.*) and acceptable catalytic activity.[14-19] However, owing to the limited electrical conductivity (10^{-5}-10^{-6} S cm^{-1}), the ORR activities of the most current MnO_2 electrocatalysts are still insufficient and needed to further boost.

To improve the ORR performance of MnO_2, many strategies including nanostructuring,[20] integrating with highly conductive materials,[21,22] doping with cations,[23,24] coating with metal nanoparticles,[25,26] introducing native oxygen defects[27] and hydrogenation,[28] have been proposed. Among these strategies, designing MnO_2 nanostructures with rational architecture and desired phase have been emerging as one of the most effective approaches to boost their electrocatalytic ORR activity. For instance, free-standing and ultrathin α-MnO_2 nanoflakes synthesized by a cationic surfactant assistant method showed a good ORR mass activity of 21 ± 1.2 mA mg^{-1} at 0.75 V vs. RHE.[20] The oxygen-deficient β-MnO_2 nanorods exhibited approximately 50 mV (vs. RHE) higher potential than the pristine β-MnO_2 nanorods.[27] Overall, these synthetic methods often require relatively complicated processes and the catalytic durability of these MnO_2-based catalysts is not yet satisfactory. More importantly, the effect of the phase variation on the ORR activity of MnO_2 is still not clear since it is difficult to obtain similar MnO_2 morphology with different crystal phases through the current synthetic approaches. Therefore, the development of a facile and effective method to prepare nanostructured MnO_2 electrocatalysts with controllable crystal phase and morphology as well as high ORR activity is of great interest and greatly challenging.

[a] Key Laboratory of Clean Chemistry Technology of Guangdong Regular Higher Education Institutions, School of Chemical Engineering and Light Industry, Guangdong University of Technology, Guangzhou 510006, P. R. China. E-mail: gych@gdut.edu.cn (Lin Yu).
[b] MOE of the Key Laboratory of Bioinorganic and Synthetic Chemistry, School of Chemistry, Sun Yat-Sen University, Guangzhou 510275, P. R. China. E-mail: luxh6@mail.sysu.edu.cn (Xihong Lu).
[c] GuangDong MeiZhou Quality & Metrology Supervision and Testing Institution, Meizhou 514072, P. R. China.
Electronic Supplementary Information (ESI) available: See DOI: 10.1039/x0xx00000x

View Article Online
DOI: 10.1039/C6TA04530H

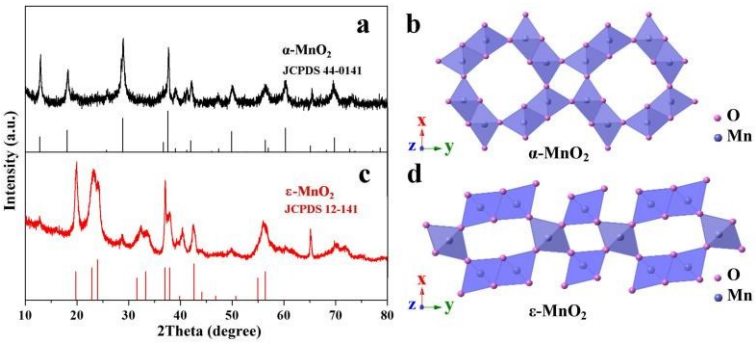

Fig. 1 XRD patterns and structural illustrations of the (a and b) α-MnO_2 (consists of double chains of edge-sharing octahedra)[33] and (c and d) ε-MnO_2 samples (consists of single and double MnO_6 octahedral chains)[34]: view along the c-axis.

Three-dimensional (3D) hierarchical architectures, assembling from one-dimensional (1D) or two-dimensional (2D) micro/nanoscale building blocks, not only can provide high surface area and fast pathway for ion diffusion and charge,[29,30] but also prevent ostwald ripening or agglomeration of the catalyst.[31] Such these features make them highly promising as electrocatalysts for ORR.[32] Herein, we demonstrated for the first time that the facile synthesis of 3D star-like MnO_2 hierarchical architectures with tunable crystal phase based on a simple redox reaction and their implementation as advanced electrocatalysts for ORR. The novel 3D α-MnO_2 and ε-MnO_2 hierarchical stars were readily achieved by a direct redox reaction using $KClO_3$/$NaClO_3$ and $Mn(CH_3COO)_2$ as precursors under mild conditions. Significantly, the resulting MnO_2 hierarchical stars presented a close relationship between the phase and ORR activity. The α-MnO_2 hierarchical stars exhibited substantially superior ORR performance than the ε-MnO_2 hierarchical stars in alkaline medium, with a more positive onset potential of 0.84 V and higher diffusion-limiting current of 5.67 mA cm^{-2}. Furthermore, the α-MnO_2 stars also had remarkably pronounced durability with more than 93.3 % retention after 10 h.

Results

Structures and morphologies

As illustrated in Fig. S1, the α-MnO_2 and ε-MnO_2 star-like hierarchical architectures were prepared via a direct redox reaction by using $KClO_3$/$NaClO_3$ and $Mn(CH_3COO)_2$ as precursors under acidic conditions, respectively. X-ray diffraction (XRD) studies were firstly conducted to investigate the phase of the products (Fig. 1a and c). Interestingly, all the reflections for the sample obtained by using $KClO_3$ as the oxidant can be well indexed to a tetragonal α-MnO_2 (JCPDS 44-0141), which possesses a 2 × 2 tunnel structure in Fig. 1b. When using $NaClO_3$ as the oxidant, a hexagonal ε-MnO_2 (JCPDS 12-141) with an intergrowth of 1 × 1 tunnels and 1 × 2 tunnels (Fig. 1d) was obtained. This indicates that the crystal phase of the MnO_2 can be readily tuned by elaborately choosing the oxidant. Fig. 2 shows the typical field emission scanning electron microscopy (FESEM) images of the α-MnO_2 and ε-MnO_2 samples. Both the MnO_2 samples exhibit a homogenous 3D star-like hierarchical architecture that consists of six branches. The α-MnO_2 hierarchical stars have a typical size of about 40-50 μm (Fig. 2a), while the ε-MnO_2 hierarchical stars have a typical size of 10-25 μm (Fig. 2c). Further observations reveal that every branch of both the MnO_2 samples is composed of parallel arrays of MnO_2 nanowires, and the angle between every pair of adjacent branches is nearly 60° (Fig. 2b and d). The surfaces of the α-MnO_2 and ε-MnO_2 hierarchical stars are relatively smooth (Fig. S2). Additionally, the big difference between these two MnO_2 samples is that the length of the α-MnO_2 branched nanowires (~ 25 μm) is substantially longer than that of the ε-MnO_2 branched nanowires (~ 13 μm). All these results fully confirmed that similar 3D MnO_2 hierarchical stars with controllable crystal phase were successfully prepared via this simple approach.

To acquire more detailed structural information of α-MnO_2 and ε-MnO_2 hierarchical stars, transmission electron microscopy (TEM) and selected area electron diffraction (SAED) analyses were carried out. Fig. 3a and 3c show the typical TEM images of an individual six-branched α-MnO_2 and

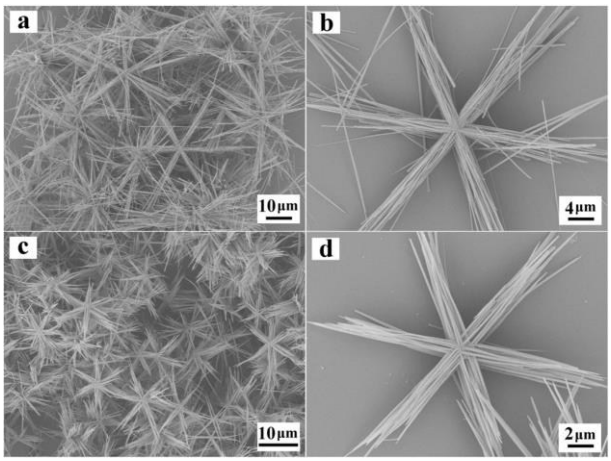

Fig. 2 FESEM images of the as-prepared MnO_2 samples: (a, b) α-MnO_2 and (c, d) ε-MnO_2.

ε-MnO_2 hierarchical star, respectively. The HRTEM image of a single nanowire on α-MnO_2 branches shows two sets of lattice spacings of 4.89 Å and 2.74 Å with an angle of 73° that correspond to the (200) and (101) planes (Fig. 3b), suggesting that the nanowire grows along the [001] direction. The three bright spots from the circle could be well indexed to (-101), (101), and (400) planes (inset of Fig. 3b). The zone axis is [010]. The SAED pattern also confirms that the nanowire is a single crystal of α-MnO_2. Fig. 3d shows the HRTEM image of a single ε-MnO_2 nanowire. The lattice spacings of 2.42 Å and 2.42 Å with an angle of 60° are in good agreement with the (100) and (010) planes, indicating the nanowire has a growth direction along of [001]. The three bright spots in the SAED pattern (inset of Fig. 3d) could be corresponded to the (-110), (010), and (100) planes. Additionally, the ε-MnO_2 nanowire is also single crystalline, which is confirmed by the well-arranged spots in the SAED pattern.

Precise control the reaction parameters such as the reaction temperature, dwell time and anion type are the key factors for the formation of uniform hierarchical nanostructures, since these parameters significantly affect their nucleation and growth process. As shown in Fig. S3, various reaction temperatures (120, 140 and 180 ℃) were applied to study the effect of temperature on the morphology of the MnO_2 products with other parameters unchanged. At lower reaction temperatures (120 and 140 ℃), the products prepared by using $KClO_3$ as the oxidant are both the urchin-like MnO_2 nanostructures (Fig. S3a and S3b), while the products obtained by using $NaClO_3$ as the oxidant are both made up of the urchin-like and star-like MnO_2 nanostructures (Fig. S3d and S3e). In general, increasing the reaction temperature will facilitate the homogeneous nucleation and growth of nanostructures,[35] thus the uniform 3D MnO_2 hierarchical stars can be formed at 160 ℃. However, when the reaction temperature further increased to 180 ℃, only rod-like MnO_2 nanostructures are observed for the products prepared by using the two different oxidants (Fig. S3e and S3f). This is because higher temperature (180 ℃) leads to a faster nucleation and growth of nanostructures, which can destroy the star-like shapes during the violently reaction.[36] Similar results were obtained for α-MnO_2 flower-like particles and CoOOH flower-like nanostructures synthesized at moderate temperature.[36,37] Moreover, we also investigated the effect of anion on the morphology of the MnO_2 products. With other conditions kept the same, the 3D MnO_2 hierarchical stars with six branches of MnO_2 nanowires can't be observed when the other kinds of anions (SO_4^{2-}, Cl^- and NO_3^-) were used in our system (Fig. S4), indicating the $CHCOO^-$ play a key role in the formation of the MnO_2 star-like shapes. Under the hydrothermal system, the carbonyl groups from CH_3COO^- could form hydrogen bond with the surface OH groups of the MnO_2 nanostructures.[38] Thus the lateral growth of MnO_2 can be restricted through the steric effects, resulting in the MnO_2 nanowires with high aspect ratios of the MnO_2 hierarchical stars.[39]

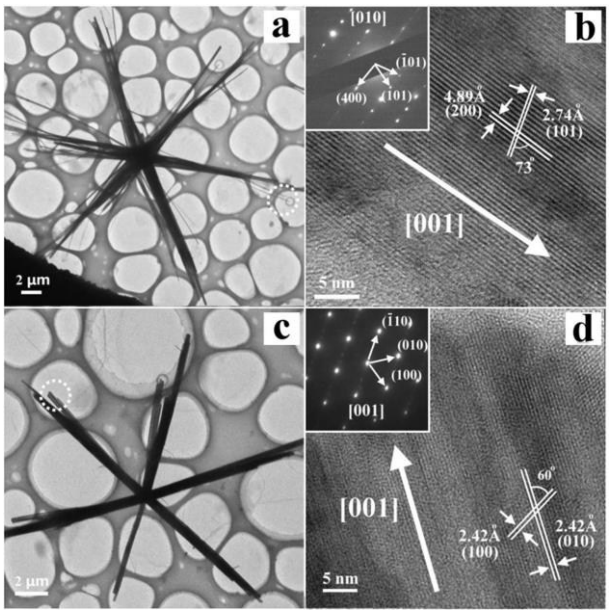

Fig. 3 TEM images and HRTEM images of (a, b) α-MnO_2 and (c, d) ε-MnO_2 hierarchical stars. The insets show the corresponding SAED patterns.

In order to understand the formation mechanism of these MnO_2 hierarchical stars, time-dependent studies were performed and the results are shown in Fig. S5 and Fig. S6. Based on the FESEM results of the 3D MnO_2 star-like hierarchical architectures after various reaction times, we proposed these MnO_2 hierarchical stars may grow according to a "nucleation-growth" process. In the early stage, primary nucleation occurs in solution, followed by producing lots of MnO_2 units spontaneously. Afterward, aggregation of the MnO_2 units will then occur to generate relatively small 3D MnO_2 nanostructures. Since the difference in the redox potentials between ClO_3^-/Cl and MnO_2/Mn^{2+} is small (~ 0.227 eV), the reaction may proceed very mildly, allowing the MnO_2 intermediates to grow slowly and homogeneously. Then, the nanorods growing from the core start to convert to the nanowires with high aspect ratios, and the 3D MnO_2 nanostructures evolve into the novel star-like hierarchical nanostructures. Finally, prolonged reaction time results in the formation of the MnO_2 hierarchical stars. A similar process has been observed in the formation of 3D MnO_2 nanostructures under the hydrothermal method.[34,40] In our experiments, the reaction conditions remained the same except for the type of oxidizing reagent. Generally, the size of the inorganic cations is believed to have a critical impact on the formation of different MnO_2 crystal phases. The cations with large sizes (such as K^+, Rb^+ and Ba^{2+}) can serve as a template to stabilize the 2 × 2 tunnel structure, while the Na^+ ions are beneficial for the synthesis of the MnO_2 structure with an intergrowth of 1 × 1 and 1 × 2 tunnels.[40] Therefore, the α-MnO_2 and ε-MnO_2 hierarchical stars with tunable crystal phase can be readily obtained under our synthesis conditions.

Electrocatalytic results

View Article Online
DOI: 10.1039/C6TA04530H

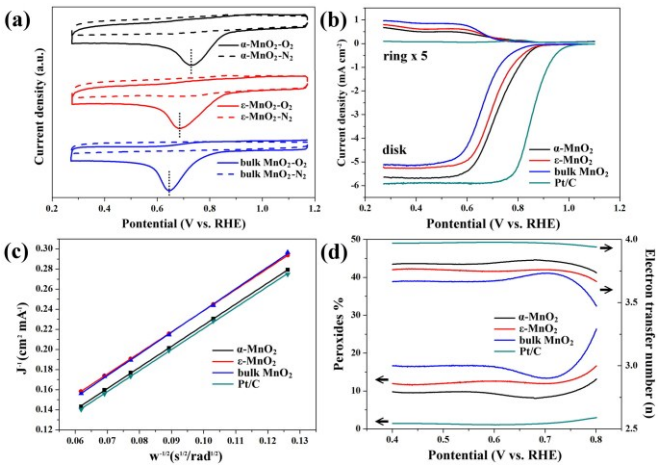

Fig. 4 (a) CV curves of the MnO_2 catalysts in both N_2-saturated and O_2-saturated 0.1 M KOH solution; (b) Polarization curves of bulk MnO_2, ε-MnO_2, α-MnO_2 and Pt/C at 1600 rpm; (c) K-L plots of the different samples at 0.45 V. (d) Electron transfer number and H_2O_2 production yield determined from RRDE data.

The electrocatalytic activity of the MnO_2 samples for the ORR was tested in 0.1 M KOH solution saturated with high-purity O_2. Fig. 4a compares the typical cyclic voltammograms (CVs) of the α-MnO_2 hierarchical stars, ε-MnO_2 hierarchical stars and bulk MnO_2 (Fig. S7) in N_2- and O_2- saturated solution at a scan rate of 50 mV s^{-1}. The CV curves of the three MnO_2 samples in N_2-saturated solution exhibit no obvious peaks, while the CV curves in the O_2-saturated have a distinct cathodic peak. Note that the cathodic peak for α-MnO_2 sample is located at 0.72 V, which is more positive than those of ε-MnO_2 sample (0.69 V) and bulk MnO_2 (0.64 V), indicating the superior electrocatalytic activity of the α-MnO_2 sample. The ORR activity of the as-prepared α-MnO_2 and ε-MnO_2 catalysts were further characterized using rotational ring-disk-electrode (RRDE) at different rotating speeds. These results were also compared with those of bulk MnO_2 and Pt/C (20 wt%). As shown in Fig. S8, all these catalysts exhibit substantial rise in limiting current densities as the rotation speeds continually enhance due to the increased mass transport at the electrode surface. Fig. 4b compares the typical LSV curves of the different catalysts recorded at 1600 rpm in 0.1 M KOH solution saturated with O_2. Significantly, the α-MnO_2 hierarchical stars yielded a more positive onset potential (E_{onset}) and larger limiting current density (around 0.84 V and 5.67 mA cm^{-2}, respectively) than those of the ε-MnO_2 hierarchical stars (around 0.80 V and 5.28 mA cm^{-2}, respectively) and bulk MnO_2 (around 0.75 V and 5.10 mA cm^{-2}, respectively). In addition, the half-wave potential ($E_{1/2}$) for α-MnO_2 sample is ~ 0.72 V, which is the highest of the three MnO_2 samples. The electrocatalytic performances (E_{onset} and $E_{1/2}$) of the α-MnO_2 hierarchical stars are comparable to those of recently reported non-precious ORR catalysts, which are summarized in Table S1. However, compared with the Pt/C catalyst, the ORR activity of the α-MnO_2 hierarchical stars is not ideal and still needed to improve. Fig. 4c depicts the Koutecky-Levich (K-L) curves derived from rotation-rate-dependent currents at 0.45 V, showing a good linearity for both α-MnO_2 and ε-MnO_2 samples. The corresponding slopes are very similar for the Pt/C, implying an apparent quasi-four-electron mechanism for these two MnO_2 samples.

The electron transfer number (n) and peroxide yields ($y_{peroxide}$) are two indicators to evaluate the ORR catalytic performance. As shown in Fig. 4d, the determined yield of peroxide species and n vary with disk potential. From 0.4 to 0.8 V, n is well approaches 3.81 for the α-MnO_2 sample and 3.77 for the ε-MnO_2 sample, again confirming the ORR with both of the two MnO_2 samples is an apparent quasi-four-electron process. Moreover, the $y_{peroxide}$ for α-MnO_2 sample is substantially lower than those of ε-MnO_2 sample and bulk MnO_2, further indicating the superior ORR activity of the α-MnO_2 hierarchical stars. Fig. S9 shows the Tafel plots of the α-MnO_2 and ε-MnO_2 samples. Obviously, two Tafel slopes can be observed for both MnO_2 samples at high and low overpotentials, respectively. The small Tafel slope is advantageous for practical catalytic applications, since it leads to a rapid increase of ORR rate with overpotential.[41] The calculated Tafel slopes for the α-MnO_2 sample are about 78 mV/dec in low overpotential range and 138 mV/dec in high overpotential range, which are distinctly smaller than those of the ε-MnO_2 sample (95 mV/dec in low overpotential range and 141 mV/dec in high overpotential range). This indicates the faster ORR reaction kinetics of the α-MnO_2 sample.

Besides the excellent catalytic activity, the α-MnO_2 hierarchical stars also show favourable catalytic stability in alkaline solution (Fig. 5). In a continuous polarization period of 10 h, more than ~ 93.3 % of the initial current is retained for the α-MnO_2 catalyst, while only ~ 78.7 % retention for the ε-MnO_2 catalyst and ~ 64.5 % for the bulk MnO_2. This present stability also outperforms the value of the Pt/C catalyst for ORR (~ 87.9 % retention after 10 h). The high durability of the α-MnO_2 hierarchical stars could be attributed to their unique 3D star-like morphology constructed by nanowires, providing some advantage against particulate agglomeration.[42] However, the durability of the ε-MnO_2 hierarchical stars is not ideal, which may be ascribed to its unstable chemical stability causing by a trace amount of dissolved MnO_2.[43,44] The gradual decay of reduction current may be due to the chemical stability of the catalysts during the ORR test. Moreover, the α-MnO_2

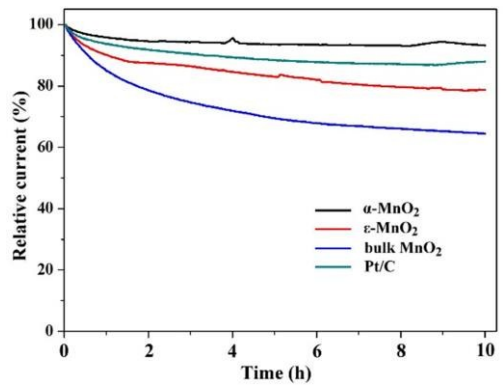

Fig. 5 Chronoamperometry of the catalysts maintained at a constant potential of 0.5 V in O_2 saturated 0.1 M KOH.

hierarchical stars were further examined by a CV test from 0.2 to -0.7 V for 2000 cycles at a scan rate of 100 mV s^{-1}. As shown in Fig. S10, there is a negative shift of ~ 29 mV in the $E_{1/2}$ value at 1600 rpm after the CV test.

In alkaline solutions, the ORR contains a series of complex electrocatalytic reactions, which is involved in several electron transfer steps. On the surface of metal catalysts, the ORR mechanism is proposed to follow by a four-electron ($4e^-$) pathway or a two-electron ($2e^-$) pathway.[23,43] As we known, MnO_2 exhibits outstanding activity toward the HO_2^- decomposition and/or reduction, thus the ORR pathway on the surface of MnO_2 could be recognized as an apparent $4e^-$ reduction mechanism involving the following steps:[45,46]

$$MnO_2 + H_2O + e^- \leftrightarrow MnOOH + OH^-$$
$$MnOOH + O_2 \leftrightarrow MnOOH \cdots O_{2,ads}$$
$$MnOOH \cdots O_{2,ads} + e^- \leftrightarrow HO_2^- + MnO_2$$
$$HO_2^- + H_2O + 2e^- \leftrightarrow 3OH^-$$
$$\text{Or } HO_2^- \leftrightarrow OH^- + O_2$$

Accordingly, we can speculate that the ORR pathway on the surface of the 3D MnO_2 hierarchical stars also follows the apparent $4e^-$ reduction mechanism because of their RRDE results (high values of n and low yields of HO_2^-). The adsorbed O_2 to replace adsorbed OH^- is considered to be the rate-limiting step of this mechanism.[45]

The ORR performance is largely determined by the surface area, morphology, size, composition and crystal structure of the MnO_2 catalysts. To gain the insights into the enhanced ORR performance of the α-MnO_2 hierarchical stars, various physicochemical characterization techniques were performed. Fig. S11 displays the N_2 adsorption-desorption isotherms of the two MnO_2 samples. It can be seen that both of the two MnO_2 samples show a characteristic of type II isotherm pattern with a hysteresis loop of type H3, suggesting the existence of slit-shaped capillaries with parallel plates.[47] Additionally, the Brunauer-Emmett-Teller (BET) surface areas were measured to be 14.9 and 17.8 m^2 g^{-1} for α-MnO_2 and ε-MnO_2, respectively, and the average pore diameter calculated by Barrete-Joyniere-Halenda (BJH) method for α-MnO_2 and ε-MnO_2 is about 12.10 and 13.55 nm (Fig. S12). Generally, the electrocatalyst with larger surface area may have more active sites on its surface for the contact with the reactants, resulting in the higher ORR activity.[26] However, our results reveal that the α-MnO_2 and ε-MnO_2 samples have close surface area and pore size, which suggests the difference in ORR activities between the two MnO_2 samples may be due to the other factors such as the O_2 adsorption affinity and electrical conductivity.[46]

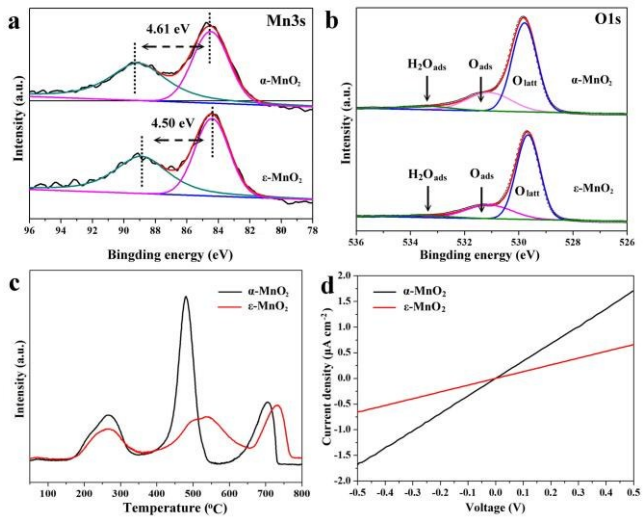

Fig. 6 XPS spectra of (a) Mn 3s and (b) O 1s for α-MnO_2 and ε-MnO_2 samples; (c) O_2-TPD profiles of the α-MnO_2 and ε-MnO_2 samples; (d) Comparison of the I-V curves of the two MnO_2 samples.

X-ray photoelectron spectroscopy (XPS) was employed to determine the chemical state of the surface Mn and O elements. Fig. S13 shows the core level Mn 2p XPS spectra of the α-MnO_2 and ε-MnO_2 samples. Two peaks, corresponding to the binding energies (BEs) of Mn $2p_{3/2}$ and Mn $2p_{1/2}$, are observed in the Mn 2p spectra. The BEs values of Mn $2p_{3/2}$ for both two MnO_2 samples are larger than 642.0 eV, indicating their oxidation states are close to +4.[48,49] The typical Mn 3s XPS spectra of the α-MnO_2 and ε-MnO_2 samples are presented in Fig 6a. The energy separation (ΔE) of α-MnO_2 sample (4.61 eV) is larger than that of ε-MnO_2 sample (4.50 eV), revealing the Mn oxidation state in α-MnO_2 sample is lower than the ε-MnO_2 sample.[50] Detailed studies have shown that the multiplet splitting energy (ΔE) of the Mn 3s decreases monotonically with the increase of the average oxidation state (AOS) of Mn element.[51] The AOS for the α-MnO_2 and ε-MnO_2 samples can be calculated to be 3.74 and 3.87, respectively.[52,53] Thus, the α-MnO_2 may have more surface oxygen vacancies than ε-MnO_2 according to the principle of electroneutrality, indicating more multivalent Mn cations in α-MnO_2 hierarchical stars.[42,54] On the other hand, the O1s spectra can be fitted into three peaks (Fig. 6b). The peaks at 529.7 eV, 531.1 eV and 533.4 eV are corresponding to the lattice oxygen (O_{latt}), surface absorbed oxygen (O_{ads}) and adsorbed H_2O (H_2O_{ads}), respectively.[28] After making quantitative analysis, the ratio of O_{ads}/O_{latt} for α-MnO_2 (0.38) is bigger than that of the ε-MnO_2 (0.32), implying a stronger interaction between the α-MnO_2 hierarchical stars and adsorbed oxygen species since the surface oxygen vacancies can be the active centers in adsorbing the oxygen molecules. The O1s XPS spectra results indicate that the α-MnO_2 sample possesses higher O_2 adsorption affinity than the ε-MnO_2 sample. As indicated in the proposed ORR pathway, the strong adsorption of O_2 on the active centers can be expected to promote the rate-limiting step, leading to the faster kinetics of the α-MnO_2 hierarchical stars.[24]

The O_2 temperature-programmed desorption (O_2-TPD) spectra of the α-MnO_2 and ε-MnO_2 hierarchical stars were collected in Fig. 6c to further understand their O_2 adsorption affinities. On the whole, the oxygen desorption peaks below 400 ℃ are attributed to the release of O_{ads}, while the desorption peaks above 400 ℃ are caused by the release of O_{latt}.[55,56] Accordingly, the α-MnO_2 sample displays much stronger peak from 150 to 400 ℃ corresponding to the O_{ads} species than that of the ε-MnO_2 sample, indicating that O_2 is preferentially absorbed on α-MnO_2 hierarchical stars. This improved O_2 adsorption capability of the α-MnO_2 hierarchical stars again

confirms the above XPS results, which is highly favorable for promoting the rate of ORR.[57] Moreover, we measured the electrical conductivity of the as-prepared MnO_2 samples by two-point current-potential (I-V) curves in a typical two electrode system. As illustrated in Fig. 6d, the current density of the α-MnO_2 sample is substantially higher than that of the ε-MnO_2 sample at the same potential, demonstrating the α-MnO_2 hierarchical stars possess superior conductivity. The enhanced electrical conductivity of the α-MnO_2 hierarchical stars can be ascribed to its higher concentration of surface oxygen vacancies, leading to the fast electron transfer and reduce electrode polarization during the ORR process.[50]

Conclusions

In summary, 3D α-MnO_2 and ε-MnO_2 hierarchical stars with similar morphology and desirable phase have been successfully synthesized via a facile redox reaction, and their possible formation mechanism were seriously investigated. It was found that the reaction temperature, anion type and dwell time played a significant role in controlling the morphologies of the MnO_2 products. These 3D hierarchical stars offer abundant active sites on the surface of the MnO_2 and prevent their aggregation as well as facilitate the O_2/electrolyte diffusion during the oxygen reduction process. Benefiting from the improved O_2 adsorption capability and conductivity, the α-MnO_2 hierarchical stars presented remarkably enhanced ORR activity compared to the ε-MnO_2 hierarchical stars and the bulk MnO_2. It achieved a more positive ORR onset potential of 0.84 V and higher diffusion-limited current of 5.67 mA cm^{-2} with excellent long-term durability. Our present findings not only afford a reliable synthetic approach to precisely prepare the 3D MnO_2 hierarchical architectures with different crystallographic forms for studying the phase-ORR activity of the electrocatalysts, but also provide new insights into design high-efficient MnO_2 catalysts for ORR.

Acknowledgements

This work was financially supported by the National Natural Science Foundation of China (21306026, 21576054, 21403306), the Scientific Project of Guangdong Province (2014A010106030, 2016A010104017), the Foundation of Higher Education of Guangdong Province (2013CXZDA016, 2013LYM0024, 2015KTSCX027).

Notes and references

1 L. Qian, L. Gu, L. Yang, H. Yuan and D. Xiao, *Nanoscale*, 2013, **5**, 7388.
2 W. Huang, H. Wang, J. Zhou, J. Wang, P. N. Duchesne, D. Muir, P. Zhang, N. Han, F. Zhao, M. Zeng, J. Zhong, C. Jin, Y. Li, S. T. Lee and H. Dai, *Nat. Commun.*, 2015, **6**, 10035.
3 L. Jin, L. Xu, C. Morein, C.-h. Chen, M. Lai, S. Dharmarathna, A. Dobley and S. L. Suib, *Adv. Funct. Mater.*, 2010, **20**, 3373.
4 H. Wang, Y. Yang, Y. Liang, G. Zheng, Y. Li, Y. Cui and H. Dai, *Energy Environ. Sci.*, 2012, **5**, 7931.
5 Z. L. Wang, D. Xu, J. J. Xu and X. B. Zhang, *Chem. Soc. Rev.*, 2014, **43**, 7746.
6 M. K. Debe, *Nature*, 2012, **486**, 43.
7 L. Zhang, M. Wei, S. Wang, Z. Li, L.-X. Ding and H. Wang, *Chem. Sci.*, 2015, **6**, 3211.
8 J. Xiao, Q. Kuang, S. Yang, F. Xiao, S. Wang and L. Guo, *Sci. Rep.*, 2013, **3**, 2300.
9 D. Chen, C. Chen, Z. M. Baiyee, Z. Shao and F. Ciucci, *Chem. Rev.*, 2015, **115**, 9869.
10 J. Xiao, C. Chen, J. Xi, Y. Xu, F. Xiao, S. Wang and S. Yang, *Nanoscale*, 2015, **7**, 7056.
11 Y. Meng, D. Voiry, A. Goswami, X. Zou, X. Huang, M. Chhowalla, Z. Liu and T. Asefa, *J. Am. Chem. Soc.*, 2014, **136**, 13554.
12 J. Y. Cheon, J. H. Kim, J. H. Kim, K. C. Goddeti, J. Y. Park and S. H. Joo, *J. Am. Chem. Soc.*, 2014, **136**, 8875.
13 Z. Chen, D. Higgins, A. Yu, L. Zhang and J. Zhang, *Energy Environ. Sci.*, 2011, **4**, 3167.
14 W. Xiao, D. Wang and X. W. Lou, *J. Phys. Chem. C*, 2010, **114**, 1694.
15 R. B. Valim, M. C. Santos, M. R. V. Lanza, S. A. S. Machado, F. H. B. Lima and M. L. Calegaro, *Electrochim. Acta*, 2012, **85**, 423.
16 K. Selvakumar, S. M. Senthil Kumar, R. Thangamuthu, K. Ganesan, P. Murugan, P. Rajput, S. N. Jha and D. Bhattacharyya, *J. Phys. Chem. C*, 2015, **119**, 6604.
17 L. Li, X. Feng, Y. Nie, S. Chen, F. Shi, K. Xiong, W. Ding, X. Qi, J. Hu, Z. Wei, L.-J. Wan and M. Xia, *ACS Catalysis*, 2015, **5**, 4825.
18 I. M. Mosa, S. Biswas, A. M. El-Sawy, V. Botu, C. Guild, W. Song, R. Ramprasad, J. F. Rusling and S. L. Suib, *J. Mater. Chem. A*, 2016, **4**, 620.
19 Y. Meng, W. Song, H. Huang, Z. Ren, S. Y. Chen and S. L. Suib, *J. Am. Chem. Soc.*, 2014, **136**, 11452.
20 C. Wei, L. Yu, C. Cui, J. Lin, C. Wei, N. Mathews, F. Huo, T. Sritharan and Z. Xu, *Chem. Commun.*, 2014, **50**, 7885.
21 J. S. Lee, G. S. Park, H. I. Lee, S. T. Kim, R. Cao, M. Liu and J. Cho, *Nano letters*, 2011, **11**, 5362.
22 T. N. Lambert, D. J. Davis, W. Lu, S. J. Limmer, P. G. Kotula, A. Thuli, M. Hungate, G. Ruan, Z. Jin and J. M. Tour, *Chem. Commun.*, 2012, **48**, 7931.
23 I. Roche, E. Chaînet, M. Chatenet and J. Vondrák, *J. Phys. Chem. C*, 2007, **111**, 1434.
24 D. J. Davis, T. N. Lambert, J. A. Vigil, M. A. Rodriguez, M. T. Brumbach, E. N. Coker and S. J. Limmer, *J. Phys. Chem. C*, 2014, **118**, 17342.
25 W. Sun, A. Hsu and R. Chen, *J. Power Sources*, 2011, **196**, 4491.
26 F. Cheng, Y. Su, J. Liang, Z. Tao and J. Chen, *Chem. Mater.*, 2010, **22**, 898.
27 F. Cheng, T. Zhang, Y. Zhang, J. Du, X. Han and J. Chen, *Angew. Chem., Int. Ed.*, 2013, **52**, 2474.
28 T. Zhang, F. Cheng, J. Du, Y. Hu and J. Chen, *Adv. Energy. Mater.*, 2015, **5**, 1400654.
29 Z. Sun, J. H. Kim, Y. Zhao, F. Bijarbooneh, V. Malgras, Y. Lee, Y. M. Kang and S. X. Dou, *J. Am. Chem. Soc.*, 2011, **133**, 19314.
30 R. Chen, H.-Y. Wang, J. Miao, H. Yang and B. Liu, *Nano Energ.*, 2015, **11**, 333.
31 Y. Xu and B. Zhang, *Chem. Soc. Rev.*, 2014, **43**, 2439.
32 Y. Fan, P.-F. Liu, Z.-W. Zhang, Y. Cui and Y. Zhang, *J. Power Sources*, 2015, **296**, 282.
33 E. M. Benbow, S. P. Kelly, L. Zhao, J. W. Reutenauer and S. L. Suib, *J. Phys. Chem. C*, 2011, **115**, 22009.
34 Y. S. Ding, X. F. Shen, S. Gomez, H. Luo, M. Aindow and S. L. Suib, *Adv. Funct. Mater.*, 2006, **16**, 549.

View Article Online
DOI: 10.1039/C6TA04530H

35 J. Yuan, W.-N. Li, S. Gomez and S. L. Suib, *J. Am. Chem. Soc.*, 2005, **127**, 14184.
36 Y. Wang, M. Liu, K. Li, A. Zhang and X. Guo, *CrystEngComm*, 2015, **17**, 3636.
37 W. J. Lan, C. C. Kuo and C. H. Chen, *Chem. Commun.*, 2013, **49**, 3025.
38 Q. Zhang, X. Cheng, X. Feng, G. Qiu, W. Tan and F. Liu, *J. Mater. Chem.*, 2011, **21**, 5223.
39 B. Lan, L. Yu, T. Lin, G. Cheng, M. Sun, F. Ye, Q. Sun and J. He, *ACS Appl. Mater. Interfaces*, 2013, **5**, 7458.
40 R. Ghosh, X. Shen, J. C. Villegas, Y. Ding, K. Malinger and S. L. Suib, *J. Phys. Chem. B*, 2006, **110**, 7592.
41 J. Du, Y. Pan, T. Zhang, X. Han, F. Cheng and J. Chen, *J. Mater. Chem.*, 2012, **22**, 15812.
42 X. Han, T. Zhang, J. Du, F. Cheng and J. Chen, *Chem. Sci*, 2013, **4**, 368.
43 W. T. Hong, M. Risch, K. A. Stoerzinger, A. Grimaud, J. Suntivich and Y. Shao-Horn, *Energy Environ. Sci.*, 2015, **8**, 1404.
44 R. Frydendal, E. A. Paoli, B. P. Knudsen, B. Wickman, P. Malacrida, I. E. L. Stephens and I. Chorkendorff, *ChemElectroChem*, 2014, **1**, 2075.
45 K. A. Stoerzinger, M. Risch, B. Han and Y. Shao-Horn, *ACS Catalysis*, 2015, **5**, 6021.
46 F. Cheng and J. Chen, *Chem. Soc. Rev.*, 2012, **41**, 2172.
47 X. Tang, Y. Li, J. Chen, Y. Xu and W. Shen, *Micropor. Mesopor. Mater.*, 2007, **103**, 250.
48 H. C. Genuino, Y. Meng, D. T. Horvath, C.-H. Kuo, M. S. Seraji, A. M. Morey, R. L. Joesten and S. L. Suib, *ChemCatChem*, 2013, **5**, 2306.
49 M. Özacar, A. S. Poyraz, H. C. Genuino, C.-H. Kuo, Y. Meng and S. L. Suib, *Appl. Catal., A*, 2013, **462-463**, 64.
50 T. Zhai, S. Xie, M. Yu, P. Fang, C. Liang, X. Lu and Y. Tong, *Nano Energ.*, 2014, **8**, 255.
51 J.-K. Chang, M.-T. Lee, W.-T. Tsai, M.-J. Deng and I. W. Sun, *Chem. Mater.*, 2009, **21**, 2688.
52 M. Sun, B. Lan, T. Lin, G. Cheng, F. Ye, L. Yu, X. Cheng and X. Zheng, *CrystEngComm*, 2013, **15**, 7010.
53 J. Hou, Y. Z. Li, M. Mao, L. Ren and X. Zhao, *ACS Appl. Mater. Interfaces*, 2014, **6**, 14981.
54 Y. Ma, R. Wang, H. Wang, J. Key and S. Ji, *J. Power Sources*, 2015, **280**, 526.
55 V. P. Santos, M. F. R. Pereira, J. J. M. Órfão and J. L. Figueiredo, *Top. Catal.*, 2009, **52**, 470.
56 Y.-G. Yin, W.-Q. Xu, Y.-F. Shen, S. L. Suib and C. L. O'Young, *Chem. Mater.*, 1994, **6**, 1803.
57 F. Cheng, J. Shen, B. Peng, Y. Pan, Z. Tao and J. Chen, *Nat Chem*, 2011, **3**, 79.

View Article Online
DOI: 10.1039/C6TA04530H

Graphical Abstract

Phase Controllable Synthesis of Three-Dimensional Star-like MnO_2 Hierarchical Architectures as Highly Efficient and Stable Oxygen Reduction Electrocatalysts

Gao Cheng,[a] Shilei Xie,[b] Bang Lan,[c] Xiaoying Zheng,[a] Fei Ye,[a] Ming Sun,[a] Xihong Lu[b]* and Lin Yu[a]*

[a]Key Laboratory of Clean Chemistry Technology of Guangdong Regular Higher Education Institutions, School of Chemical Engineering and Light Industry, Guangdong University of Technology, Guangzhou 510006, P. R. China.

E-mail: gych@gdut.edu.cn (Lin Yu).

[b]MOE of the Key Laboratory of Bioinorganic and Synthetic Chemistry, School of Chemistry and Chemical Engineering, Sun Yat-Sen University, Guangzhou 510275, P. R. China.

E-mail: luxh6@mail.sysu.edu.cn (Xihong Lu).

[c]GuangDong MeiZhou Quality & Metrology Supervision and Testing Institution, Meizhou 514072, P. R. China.

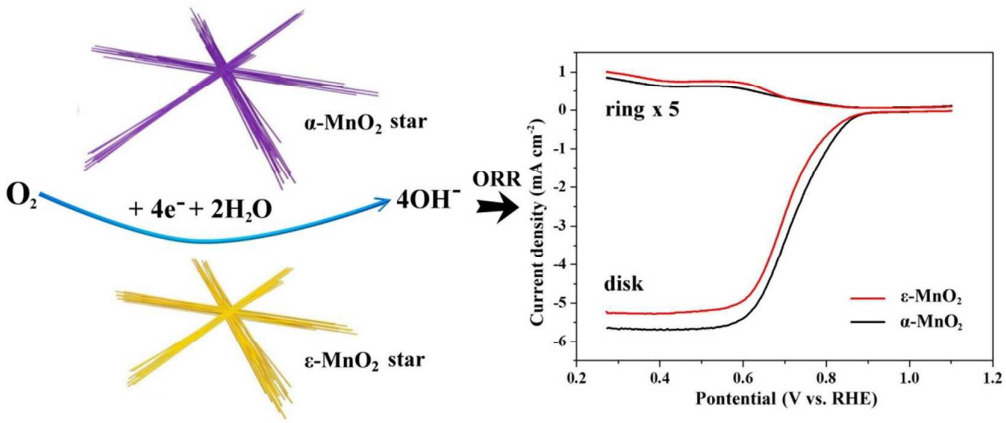

Three-dimensional (3D) α-MnO_2 and ε-MnO_2 hierarchical star-like architectures were readily prepared by a facile hydrothermal method without any surfactants or templates. The as-obtained α-MnO_2 catalyst showed substantially enhanced ORR activity compared to the ε-MnO_2 catalyst, which can be served as efficient catalysts for ORR-based applications.